Linear stability analysis of radiative effects on compressible Rayleigh-Taylor instability

Cunbo Zhang [1,2] Zongqiang Ma,[1] Yang Song,[1] Cheng-quan Fu [1] Zhengfeng Fan [1] Anmin He,[1] and Pei Wang[1,2,*]
[1]*Institute of Applied Physics and Computational Mathematics, Beijing 100088, People's Republic of China*
[2]*National Key Laboratory of Computational Physics, Beijing 100088, People's Republic of China*

(Received 6 December 2025; accepted 9 March 2026; published 1 April 2026)

Within the equilibrium-diffusion approximation for radiation, we perform a linear stability analysis of the compressible Rayleigh-Taylor instability in a stratified, isothermal background. Radiation alters the growth rate by modulating the fluid's effective compressibility. Radiative diffusion enhances compressibility, driving the growth rate from the adiabatic toward the isothermal limit as the Péclet number Pe decreases. In contrast, radiation pressure reduces compressibility, steering the growth rate toward the incompressible limit as the Mihalas number R decreases. These competing effects are governed by the key dimensionless groups Pe (convective versus diffusive transport) and R (material versus radiation pressure). The impact of radiation is most pronounced at low Atwood numbers (At), high stratification parameters (Sr), or large interface thicknesses (δ).

DOI: 10.1103/cmm2-dtwb

I. INTRODUCTION

The Rayleigh-Taylor instability (RTI)—the interfacial instability that develops when a denser fluid overlies or accelerates into a lighter one [1,2]—has attracted widespread attention across geophysical, astrophysical, and laboratory contexts [3–6] and has been investigated extensively through theory, experiment, and numerical simulation [7,8].

The influence of compressibility on the linear stage of RTI was long debated, with early studies reporting conflicting results: destabilizing effects [9–11], stabilizing effects [12–14], or both within single studies [15,16]. Livescu *et al.* [17] resolved this by demonstrating that compressibility requires two characterization parameters—the speed of sound (quantifying background stratification via Sr) and the specific heat ratio γ (governing fluid compressibility [18]). Increasing background compressibility (larger Sr) stabilizes RTI, whereas a smaller γ (stronger fluid compressibility) enhances growth rates. As $\gamma \to \infty$, growth rates approach Bernstein and Book's incompressible solution [9]: $\sigma^2 = \mathrm{Sr}(\mathrm{At}^2-1)/2+\sqrt{\mathrm{Sr}^2(\mathrm{At}^2-1)^2/4+\mathrm{At}^2}$ (where At denotes the Atwood number). Conversely, when $\gamma \to 1$—studied by Vandervoort [19], Plesset and Prosperetti [20], and Ribeyre *et al.* [21]—compressibility effects peak, dramatically enhancing instability growth.

In high-energy density (HED) environments, including astrophysical systems [22] and inertial confinement fusion (ICF) implosions [23], RTI amplification is modulated by multiphysics couplings. Mass ablation driven by localized energy deposition [24,25] and preheating induced by high-energy particle transport [26,27] have been shown to exert a significant impact on the instability. While radiation is a primary energy transport channel in HED flows, its specific influence on RTI remains largely unexplored in comparison to ablation or preheating studies.

Recently, Jacquet [28] studied the role of radiation pressure by performing linear stability analysis of RTI in two asymptotic limits: in the optically thin regime, radiation pressure acts as an effective gravitational field, while in the optically thick adiabatic regime, it modifies the equation of state. Hu [29] subsequently employed this framework to simulate nonlinear bubble evolution in optically thin plasmas. Tremblin [30], using the Boussinesq approximation, treated radiation as a heat source and performed linear stability analysis, demonstrating that an instability arises when a lower-opacity medium overlies a higher-opacity one within a decreasing temperature gradient. More recently, Chkair [31] examined Rayleigh-Taylor turbulent mixing using the equilibrium-diffusion approximation for radiative transport. Numerical simulations revealed a sharp contrast: at small Prandtl numbers—where radiative diffusion dominates—the mixing zone grew continuously, whereas high-Prandtl cases saturated. They derived an instability criterion for small-Péclet extremes, offering a theoretical explanation for the sustained growth observed in the simulations.

Collectively, existing studies indicate that radiation can alter RTI growth through either radiative heat conduction or radiation pressure. Yet the inherent complexity of radiation modeling has often led to separate treatments of these mechanisms within different frameworks, leaving a unified description of these two effects absent and the overall picture incomplete. Here, within the equilibrium diffusion approximation [31], we present a linear stability analysis (LSA) of compressible stratified RTI that simultaneously incorporates both radiation mechanisms, providing an integrated framework where their combined effect is characterized by two key parameters: the Péclet number (radiative diffusion) and the Mihalas number (radiation pressure).

Radiative diffusion is characterized by the Péclet number $\mathrm{Pe} = \mathrm{RePr}$, with Re representing the Reynolds number and

[*]Contact author: wangpei@iapcm.ac.cn

the Prandtl number Pr the ratio of kinematic viscosity to radiative thermal diffusivity. In HED regimes, the radiation-dominated thermal diffusivity exceeds the kinematic viscosity by several orders of magnitude [32], yielding exceptionally small Prandtl numbers (typical values $\sim 10^{-5}$–10^{-9} in stellar and ICF plasmas [32,33])—well below the conventional order-unity values. Low-Pr radiative effects have been studied for thermal convection [34], stratified shear [35] and double-diffusive systems [33,36], but their influence on the RTI remains largely unexplored. Radiation pressure is characterized by the Mihalas number R, defined as the ratio of material to radiation pressure. For classical gases $R \to \infty$, whereas in HED plasmas $R \lesssim 1$ and radiation pressure competes with or dominates the total pressure [22,37], the regime addressed here.

The present work builds upon the classic analysis of Livescu [17], who, in the classical fluid limit (Pe $\to \infty$, $R \to \infty$), unified the long-standing debate over whether compressibility stabilizes or destabilizes the Rayleigh-Taylor instability [9–16]. We extend that framework to the HED regime, systematically quantifying how finite radiative diffusion (Pe $\lesssim 1$) and comparable radiation pressure ($R \lesssim 1$) jointly reshape the linear growth of compressible RTI.

The organization of the article is as follows. Section II presents the LSA method. Results are presented in Sec. III, where the effects of radiative heat conduction and radiation pressure on RTI growth rate and influence of Atwood number, stratification, and interface thickness are analyzed. We finally draw conclusions in Sec. IV.

II. METHOD OF LINEAR STABILITY ANALYSIS

The linear stability of the RTI has traditionally been pursued through closed-form dispersion relations. However, incorporating compressibility and radiative effects renders the analytical approach intractable. Livescu [17] showed that the dispersion relation for compressible RTI cannot be expressed explicitly and must be obtained by solving a nonlinear equation numerically. Introducing radiation further complicates the problem, forcing severe physical simplifications if an analytical treatment is insisted upon [28]. Following the approach widely used in boundary-layer stability analysis [38], we formulate the linear stability problem as an eigenvalue system and solve it numerically, thus avoiding undue idealizations of the underlying physics.

A. Governing equations

Under the equilibrium diffusion approximation, the radiation and matter fields are characterized by a common temperature T, and the radiation energy flux obeys Fick's law of diffusion [37]. The equilibrium-diffusion approximation assumes the photon mean-free path is much smaller than the characteristic system length. The evolution of the radiative flow in this study is governed by the following equations:

$$\partial_t \rho + \partial_j(\rho u_j) = 0, \tag{1}$$

$$\rho(\partial_t u_i + u_j \partial_j u_i) = -\partial_i p - \rho g \delta_{i2}, \tag{2}$$

$$\rho(\partial_t e + u_j \partial_j e) + p \partial_j u_j = \partial_j q_j, \tag{3}$$

$$\partial_t c + u_j \partial_j c = 0, \tag{4}$$

where ρ, p, e, c denote density, pressure, internal energy, and mass fraction, respectively. u_i ($i = 1, 2$) refers to the velocity components along the x and y axes. g is the external gravitational force in the opposite direction along the y axis. The operators ∂_j and ∂_t denote partial derivatives with respect to the spatial coordinate x_j and time t, respectively. To isolate the effects of radiation, viscous and molecular diffusion terms are omitted from the governing equations.

The radiative heat flux q_j on the right-hand side of equation (3) is defined as

$$q_j = \kappa \partial_j T, \tag{5}$$

where the radiative thermal conductivity κ depends on density ρ and temperature T as $\kappa = \kappa_e \rho^\alpha T^\beta$. Typical values for these exponents in radiative conductivity models include $\alpha \in [-2, -1]$ and $\beta \in [4, 7]$, for example, $\alpha = -2$, $\beta = 6.5$ for fully ionized plasma [39]; $\alpha = -1$, $\beta = 4.33$ for Al [32]; and $\alpha = -1.3$, $\beta = 4.5$ for Au [32]. Electron thermal conduction can be incorporated within the present framework by setting $\alpha = 0$, $\beta = 2.5$.

For simplicity, we assume that the thermal conductivity of both light and heavy fluids exhibits the same functional dependence on temperature and density (i.e., the same exponents α and β), but with different coefficients κ_e such that $\kappa_e = \kappa_{e,h} c + \kappa_{e,\ell}(1 - c)$. Quantities for the heavy and light fluids are denoted by the subscripts h and ℓ, respectively.

The pressure p in the above equations represents the total pressure of the radiative flow, which comprises the material pressure p^{m} and the radiation pressure p^{r}. It is also the case for the internal energy, with $e = e^{\mathrm{m}} + E^{\mathrm{r}}/\rho$, where E^{r} is the volumetric energy of radiation. The material and radiation components are denoted by the upright-font superscripts m and r, respectively.

Equations for the state are needed to close the governing equations. The radiation pressure is expressed as

$$p^{\mathrm{r}} = \frac{E^{\mathrm{r}}}{3}, \quad \text{with} \quad E^{\mathrm{r}} = aT^4, \tag{6}$$

where a is the radiation constant [32].

The material pressure is formulated as

$$p^{\mathrm{m}} = \rho r^{\mathrm{m}} T, \quad \text{with} \quad r^{\mathrm{m}} = r_h^{\mathrm{m}} c + r_\ell^{\mathrm{m}}(1 - c), \tag{7}$$

where $r_h^{\mathrm{m}} = \mathscr{R}/M_h$ and $r_\ell^{\mathrm{m}} = \mathscr{R}/M_\ell$ are the gas constants for heavy and light fluids, respectively, with $\mathscr{R}$ the universal gas constant, and M_h, M_ℓ their effective molar mass.

The energy equation can be recast as an evolution equation for temperature, which is more convenient for the subsequent stability analysis:

$$\partial_t T + u_j \partial_j T = -(\gamma_2 - 1) T \partial_j u_j + \frac{\partial_j(q_j)}{\rho C_V}. \tag{8}$$

The coefficient γ_2 is the generalized adiabatic exponent defined for a continuum of matter and radiation [31,37] by

$$\gamma_2 = 1 + \frac{\rho}{T} \partial_\rho T|_{s,c} = 1 + \frac{-\rho^2 \partial_\rho e|_{T,c} + p}{\rho C_V T}, \tag{9}$$

where γ_2 equals the material adiabatic exponent γ^{m} for a perfect gas without radiation. In this study, γ^{m} is set to 5/3 for both the heavy and light fluids.

C_V in Eq. (9) denotes the total specific heat at constant volume:

$$C_V = \frac{r_h^{\mathrm{m}} c + r_\ell^{\mathrm{m}}(1-c)}{\gamma^{\mathrm{m}} - 1} + \frac{4aT^3}{\rho}. \quad (10)$$

B. Dimensionless governing equations

The governing equations from the previous subsection will be nondimensionalized below. For clarity, dimensional variables are hereafter denoted by a tilde. And the reference values at the initial interface are denoted by the subscript I. The initial material pressure $\tilde{p}_I^{\mathrm{m}}$ and temperature $\tilde{T}_I$ at the interface are used to nondimensionalize pressure and temperature, respectively. Correspondingly, the reference density is set as $\tilde{\rho}_I = \tilde{p}_I^{\mathrm{m}} \tilde{M}_I/(\tilde{\mathcal{R}}\tilde{T}_I)$, with $\tilde{M}_I = (\tilde{M}_h + \tilde{M}_\ell)/2$ denoting the effective molar masses at the interface. Atwood number is defined as $\mathrm{At} = (\tilde{\mathrm{M}}_{\mathrm{h}} - \tilde{\mathrm{M}}_\ell)/(\tilde{\mathrm{M}}_{\mathrm{h}} + \tilde{\mathrm{M}}_\ell)$. The reference length is chosen as $\tilde{L}_I = 1/\tilde{k}$, where $\tilde{k}$ is the wave number of the perturbation wave. Correspondingly, the reference time and velocity are set as $\tilde{t}_I = \sqrt{1/(\tilde{g}\tilde{k})}$ and $\tilde{u}_I = \sqrt{\tilde{g}/\tilde{k}}$, respectively. The reference radiative thermal conductivity is defined as $\tilde{\kappa}_I = \tilde{\kappa}_{e,I}(\tilde{\rho}_I)^\alpha(\tilde{T}_I)^\beta$, where $\tilde{\kappa}_{e,I} = [(1+\mathrm{At})\tilde{\kappa}_{\mathrm{e,h}} + (1-\mathrm{At})\tilde{\kappa}_{\mathrm{e},\ell}]/2$. The dimensionless governing equations are:

$$\partial_t \rho + \partial_j(\rho u_j) = 0, \quad (11)$$

$$\rho(\partial_t u_i + u_j \partial_j u_i) = -\frac{1}{\mathrm{Sr}}\partial_i p - \rho\delta_{i2}, \quad (12)$$

$$\partial_t T + u_j \partial_j T = -(\gamma_2 - 1)T\partial_j u_j + \frac{1}{\mathrm{Pe}}\frac{\partial_j(\kappa\partial_j T)}{\rho C_V}, \quad (13)$$

$$\partial_t c + u_j \partial_j c = 0, \quad (14)$$

with stratification number $\mathrm{Sr} = \tilde{g}\tilde{L}_I\tilde{\rho}_I/\tilde{p}_I^{\mathrm{m}}$ quantifying stratified compressibility and Péclet number $\mathrm{Pe} = \tilde{\rho}_I\tilde{u}_I\tilde{L}_I\tilde{\mathscr{R}}/(\tilde{\kappa}_I\tilde{M}_I)$ characterizing the relative importance of radiative thermal diffusion against convective transport.

The dimensionless specific gas constant is

$$r^{\mathrm{m}} = \frac{c}{1+\mathrm{At}} + \frac{1-c}{1-\mathrm{At}}. \quad (15)$$

Total pressure is

$$p = \rho T r^{\mathrm{m}} + \frac{1}{R}T^4 \quad (16)$$

with Mihalas number $R = \tilde{p}_I^{\mathrm{m}}/[\tilde{a}(\tilde{T}_I)^4/3]$ representing the ratio of the material pressure and the radiation pressure [32,40].

Dimensionless total specific heat is

$$C_V = \frac{1}{\gamma^{\mathrm{m}} - 1}\left(\frac{c}{1+\mathrm{At}} + \frac{1-c}{1-\mathrm{At}}\right) + \frac{12}{R}\frac{T^3}{\rho}. \quad (17)$$

The radiative thermal conductivity is nondimensionalized using the initial interface value $\tilde{\kappa}_I$ and expressed as

$$\kappa = [c\kappa_{e,h} + (1-c)\kappa_{e,\ell}]\rho^\alpha T^\beta, \quad (18)$$

where $\kappa_{e,h}$ and $\kappa_{e,\ell}$ denote the thermal conductivity coefficients of the heavy and light fluids, respectively:

$$\kappa_{e,h} = \frac{1+A_\kappa}{1+\mathrm{At}A_\kappa}, \quad (19)$$

$$\kappa_{e,\ell} = \frac{1-A_\kappa}{1+\mathrm{At}A_\kappa}, \quad (20)$$

with A_κ quantifying the relative disparity between the conductivity coefficients:

$$A_\kappa = \frac{\tilde{\kappa}_{e,h} - \tilde{\kappa}_{e,\ell}}{\tilde{\kappa}_{e,h} + \tilde{\kappa}_{e,\ell}}. \quad (21)$$

C. Stationary background state

To investigate the linear stability of the system, we consider perturbations about a stationary background state. The background state (denoted by subscript 0) is assumed to be in hydrostatic equilibrium ($u_{0,i}(y) = 0$) and thermal equilibrium [$T_0(y) = 1$] [17,31]. Widely adopted in previous studies [17,18,41–43], this initial isothermal state represents a preexisting global equilibrium assuming the background thermal relaxation time to be distinct from the perturbation growth time. Substituting these into the governing equations yields

$$p_0(y) = \exp\left(-\frac{\mathrm{Sr}y}{r_0^{\mathrm{m}} T_0}\right) + \frac{T_0^4}{R}, \quad (22)$$

$$\rho_0(y) = \frac{1}{r_0^{\mathrm{m}} T_0}\exp\left(-\frac{\mathrm{Sr}y}{\mathrm{m}_0 T_0}\right). \quad (23)$$

Note that the added background radiation pressure is uniform throughout the domain. Equations (22) and (23) hold for the pure fluid on either side of the interface. To smooth the interface, the molar fraction is defined as

$$X_0(y) = \frac{1 + \mathrm{erf}(y/\delta)}{2}, \quad (24)$$

where δ is the pseudo-interface thickness [41,44]. The mass fraction is given by

$$c_0(y) = \frac{X_0(y)(1+\mathrm{At})}{X_0(y)(1+\mathrm{At}) + [1 - X_0(y)](1-\mathrm{At})}. \quad (25)$$

The specific gas constant r_0^{m} for the stationary background state is determined by substituting Eq. (25) into Eq. (15).

While Eqs. (22) and (23) hold for uniform compositions, the smoothed interface described by Eq. (25) introduces a composition gradient. To maintain hydrostatic equilibrium in the presence of this gradient, the background pressure and density profiles are modified following Reckinger *et al.* [42], leading to

$$p_0(y) = \exp\left[\frac{-\mathrm{Sr}}{r_0^{\mathrm{m}} T_0}\left(y - \frac{\delta^2}{2}\frac{\partial \ln r_0^{\mathrm{m}}}{\partial y}\right)\right] + \frac{T_0^4}{R}, \quad (26)$$

$$\rho_0(y) = \frac{1}{r_0^{\mathrm{m}} T_0}\exp\left[\frac{-\mathrm{Sr}}{r_0^{\mathrm{m}} T_0}\left(y - \frac{\delta^2}{2}\frac{\partial \ln r_0^{\mathrm{m}}}{\partial y}\right)\right]. \quad (27)$$

As illustrated in Fig. 1, the background density profile is influenced by Sr and At.

D. Equations for the disturbances

Each instantaneous flow quantity is decomposed into a background component and a perturbation component, denoted as $\phi = \phi_0 + \phi'$ where $\phi = [\rho, u, v, T, c]$. The linearized disturbance equations are obtained by subtracting the

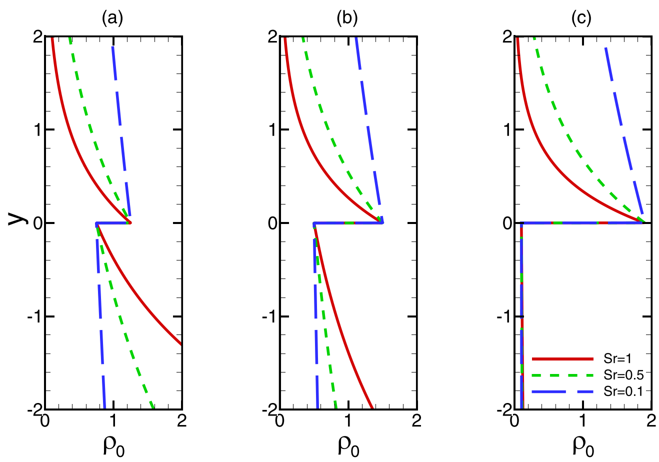

FIG. 1. Background density profiles for stratification parameters Sr and Atwood numbers At, with a fixed interface thickness parameter $\delta = 10^{-3}$: (a) At $= 0.25$, (b) At $= 0.5$, and (c) At $= 0.9$.

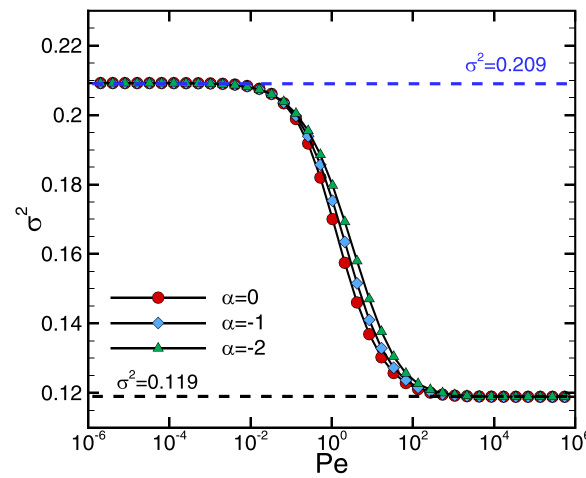

FIG. 2. Squared growth rate versus Péclet number at $R = 10^6$. Solid curves: $\kappa \propto \rho^\alpha$ with $\alpha = 0, -1$ and -2. Black dashed line: Compressible theory value; blue dashed line: compressible theory with $\gamma^m \equiv 1$.

background state equations from the instantaneous governing equations and neglecting nonlinear terms in the perturbations:

$$\partial_t \rho' + \rho_0 \partial_j u_j' + u_j' \partial_j \rho_0 = 0, \tag{28}$$

$$\rho_0 \partial_t u_i' = -\frac{1}{\mathrm{Sr}} \partial_i p' - \rho' \delta_{i2}, \tag{29}$$

$$\partial_t T' = -(\gamma_{2,0} - 1) T_0 \partial_j u_j' + \frac{1}{\mathrm{Pe}} \frac{\partial_j (\kappa_0 \partial_j T')}{\rho_0 C_{V,0}}, \tag{30}$$

$$\partial_t c' + u_j' \partial_j c_0 = 0, \tag{31}$$

where the perturbation pressure p' is expanded around the background state and linearized, $p' = \rho' \partial_\rho p_0 + c' \partial_c p_0 + T' \partial_T p_0$. Since $T_0 = 1$ and $\partial_j T_0 = 0$, $\kappa_0 = \rho_0^\alpha T_0^\beta = \rho_0^\alpha$. Thus, the exponent β vanishes in the final stability equations.

Perturbations are assumed to take the form $\phi'(y, t) = \hat{\phi}(y) \exp(ikx + \sigma t)$, where $\hat{\phi}(y)$ denotes the shape function, σ denotes the growth rate. As the length is scaled by $1/\tilde{k}$, the dimensionless wave number is unity ($k \equiv 1$). Substituting this ansatz into the disturbance equations and rearranging yields a compact eigenvalue problem:

$$(\mathbf{V} + ik\mathbf{V}_x - k^2 \mathbf{V}_{xx} + \mathbf{V}_y \partial_y + \mathbf{V}_{yy} \partial_{yy}) \hat{\phi} = -\sigma \mathbf{V}_t \hat{\phi}. \tag{32}$$

For brevity, the full expressions for the matrices $\mathbf{V}$, $\mathbf{V}_x$, $\mathbf{V}_{xx}$, $\mathbf{V}_y$, $\mathbf{V}_{yy}$, and $\mathbf{V}_t$ are detailed in Appendix A.

The eigenvalue problem Eq. (32) is discretized over a finite domain $y \in [-L_y, L_y]$ with $L_y = 7.5$, using a central difference scheme on $n_y = 1000$ grid points. To enhance interface resolution, grid points are clustered near the interface, with approximately half distributed within $|y| < 4\delta$. Dirichlet boundary conditions ($\hat{\rho} = \hat{u} = \hat{v} = \hat{T} = \hat{c} = 0$) are imposed at both domain boundaries. The resulting generalized matrix eigenvalue problem is solved for the growth rate σ using the Arnoldi iterative method [45], which yields a set of eigensolutions. The solution with the largest real part is of primary interest. To enhance computational efficiency, this solution serves as the initial guess for parameter scanning via the more efficient generalized Rayleigh quotient method [46]. Convergence studies with respect to domain size and grid resolution confirm numerical robustness, while linear stability analysis results are validated against prior nonradiative studies; both analyses are presented in Appendixes B and C.

III. RESULTS

In this section, the radiation effects on the stability of the compressible RTI are investigated using the LSA introduced previously. First, the general impacts of radiative diffusion and radiation pressure are presented at a specific set of parameters. Then, to clarify the underlying mechanism, we present a corresponding physical picture. Subsequently, the key parameters—the Atwood number, the radiative thermal conduction coefficients, and the diffusion thickness—are systematically varied to yield additional results.

A. The general impact of radiation on compressible RTI

This subsection examines the impact of radiative diffusion and radiation pressure for a typical case, with At $= 0.25$, Sr $= 1.0$, $A_\kappa = 0$, and $\delta = 10^{-3}$.

Figure 2 presents the squared growth rate versus the Péclet number across an extensive range. With the Mihalas number fixed at 10^6 (to eliminate radiation pressure effects), the figure shows that reducing the Péclet number (i.e., enhancing radiative diffusion) significantly amplifies RTI growth rate.

Figure 2 reveals two distinct asymptotic limits. As Pe $\to \infty$, radiative diffusion becomes negligible, and the RTI growth rate converges to its adiabatic limit value. This aligns with the classical compressible RTI growth rate [17]. Conversely, as Pe $\to 0$, radiative diffusion dominates, establishing an isothermal regime where the RTI growth rate approaches a significantly elevated value.

Notably, artificially adjusting the medium's compressibility by setting the specific heat ratio to unity ($\gamma^m = 1$) in both media yields a classical RTI growth rate prediction [17] that exactly matches the elevated isothermal-limit value. This indicates that radiation influences RTI growth primarily through compressibility effects.

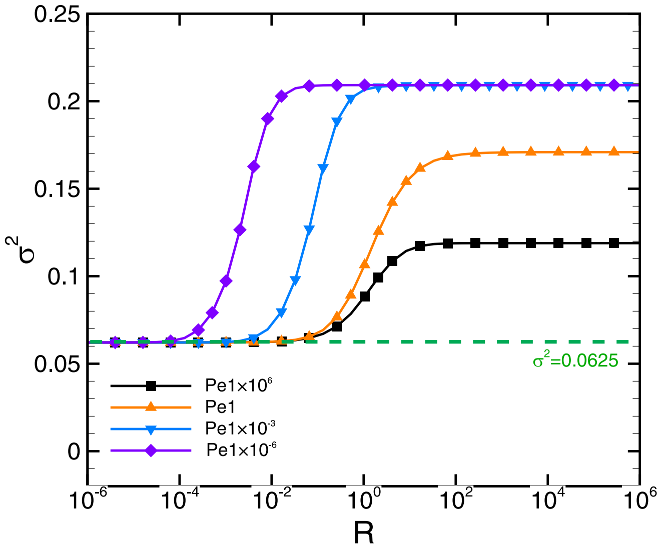

FIG. 3. Squared growth rate versus Mihalas number for varying Péclet numbers. Solid curves: LSA results; green dashed: classical compressible theory in the limit $\gamma^{\mathrm{m}} \rightarrow \infty$.

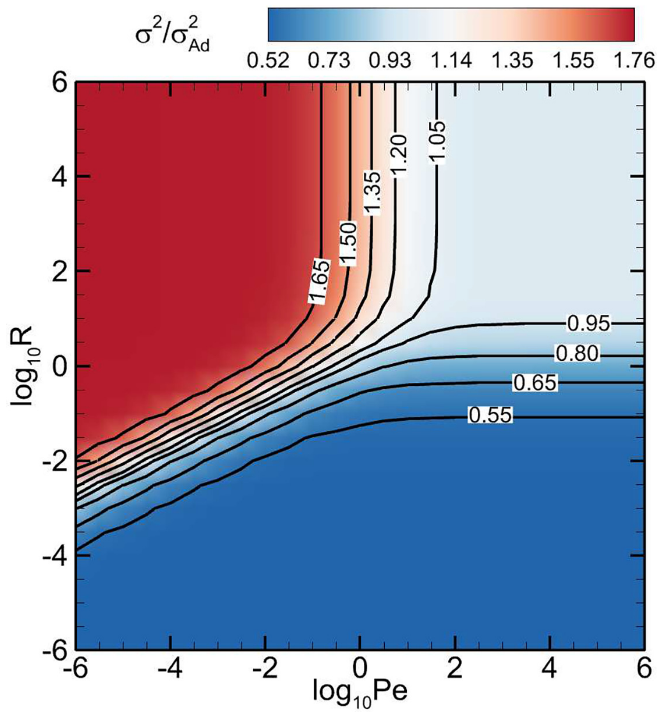

FIG. 4. Contours of the squared growth rate normalized by adiabatic limit value.

The growth-rate variation with Péclet number can be divided into three distinct stages: as long as Pe remains above $\sim 10^2$ the value stays essentially at the adiabatic limit; a further decrease in Pe causes a rapid amplification of the growth rate; and once Pe drops below $\sim 10^{-2}$ the rate asymptotes to the isothermal limit and levels off again. Livescu [17] noted that thermal conduction exerts only a minor influence on the growth rate of compressible RTI. Based on Fig. 2, we infer that their parameters were located on the plateau where $\mathrm{Pe} \gtrsim 10^2$.

Figure 2 shows growth rates for different α in $\kappa \propto \rho^{\alpha}$. Typical values $\alpha = -2, -1$ for radiative heat conductivity and $\alpha = 0$ for electron heat conductivity are checked. Varying α does not shift the asymptotic growth rate limits. For $10^{-2} < \mathrm{Pe} < 10^2$, the nonlinear conductivity (e.g., $\alpha = -2$) shows modest growth rate increases relative to constant conductivity ($\alpha = 0$). This insensitivity to conductivity exponents arises from the uniform-temperature assumption; in systems with large temperature gradients, these exponents may significantly alter dynamics [47].

This study extends to examine radiation pressure effects on the growth of RTI. Figure 3 plots the squared growth rate versus Mihalas number across multiple Péclet numbers. Critically, increasing radiation pressure (corresponding to decreasing Mihalas number) significantly suppresses RTI growth rate. As the Mihalas number asymptotically approaches zero, the perturbation growth rate converges to a new asymptotic limit. This limit value is identical to that of classical RTI when the specific heat ratio $\gamma^{\mathrm{m}} \rightarrow \infty$. This equivalence demonstrates that the observed limiting state physically corresponds to an incompressible limit.

Given the initially uniform temperature distribution, radiation pressure remains constant. Increasing radiation pressure is physically equivalent to elevating the medium's sound speed. A fundamental distinction exists between radiation and material background pressures: increased radiation pressure preserves the material profile, whereas in classical RTI, increased material pressure restores the flow to a nonstratified state. As the Mihalas number asymptotically approaches zero, the sound speed tends to infinity. Consequently, the RTI amplification process exhibits incompressible characteristics, maintaining constant densities in spikes and bubbles at initial values.

Figure 3 demonstrates that the influence of radiation pressure on the RTI growth rate correlates with the Péclet number: decreasing Pe numbers require lower Mihalas numbers for radiation pressure to become significant. To elucidate the combined effects of radiative diffusion and pressure on RTI, Fig. 4 depicts a regime diagram with growth rates normalized by the adiabatic limit value. In the red region, radiative diffusion dominates, enhancing RTI growth; in the blue region, radiation pressure dominates, suppressing growth. To illustrate the practical relevance of the parameter space explored in Fig. 4, we provide estimates of the characteristic Pe and R values across real systems, along with a parameter survey in Appendix D.

B. Physical mechanism: Modulation of compressibility

To elucidate how radiation impacts the RTI growth rate, this section presents a simplified physical model inspired by Tremblin's research [30]. As sketched in Fig. 5, we consider a fluid element initially on the heavy-fluid side adjacent to the interface. As RTI evolves, this element penetrates the underlying lighter fluid, forming a spike. With increasing spike height, the surrounding pressure rises, inducing compression—a stage where radiation plays a critical role.

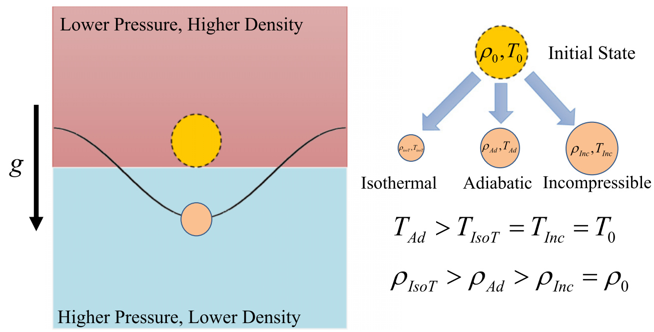

FIG. 5. Mechanism of radiation-modulated compressibility in RTI. The schematic contrasts the compression and density states of the spike: (i) strong radiative diffusion (low Pe), which cools the spike, enhancing the density contrast and buoyancy drive; and (ii) strong radiation pressure (low R), which suppresses compression and weakens the buoyancy drive.

In an adiabatic process (without radiation), compression elevates the element's temperature. Conversely, in an isothermal process (dominated by strong radiative diffusion), heat from compression is instantaneously dissipated via radiative diffusion, maintaining constant temperature. Consequently, under isothermal conditions, the heavy fluid at the spike attains a lower temperature with enhanced compressibility and higher density, while the light fluid at the bubble achieves a higher temperature with greater expandability and lower density.

This mechanism is confirmed by Fig. 6, which compares the shape functions of temperature and velocity divergence across different Péclet numbers (Pe $= 10^6$, 1, 10^{-6}). Temperature perturbations are positive in the spike region and negative in the bubble region, with amplitude suppressed as Pe decreases. Simultaneously, amplitude of velocity divergence increases, enhancing compressibility at the spike and expandability at the bubble.

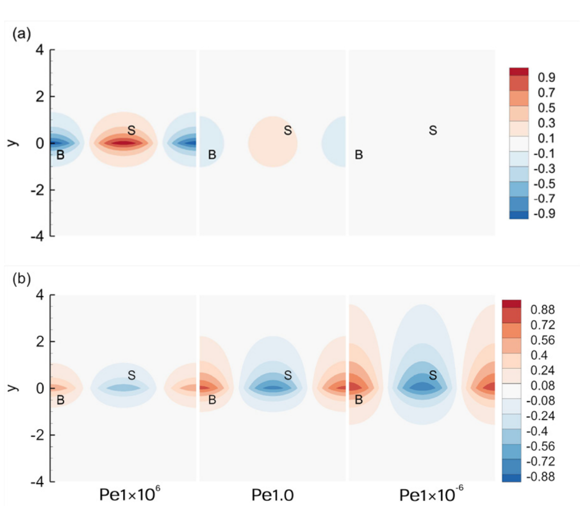

FIG. 6. Temperature ($\hat{T}e^{ikx}$) and velocity-divergence ($\partial_j \hat{u}_j e^{ikx}$) eigenfunctions, normalized by the vertical-velocity amplitude $|\hat{v}|$, for Pe $= 10^6$, 1 and 10^{-6} at At $= 0.25$, Sr $= 1$ and $R = 10^6$. The spike (S) and bubble (B) regions are marked.

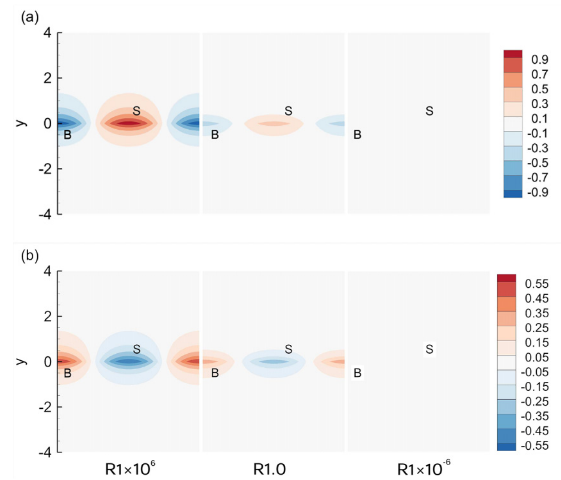

FIG. 7. Temperature ($\hat{T}e^{ikx}$) and velocity-divergence ($\partial_j \hat{u}_j e^{ikx}$) eigenfunctions, normalized by the vertical-velocity amplitude $|\hat{v}|$, for $R = 10^6$, 1 and 10^{-6} at At $= 0.25$, Sr $= 1$ and Pe $= 10^6$. The spike (S) and bubble (B) regions are marked.

Crucially, this higher-density spike and lower-density bubble signify a stronger buoyancy effect, which directly amplifies RTI growth. In summary, radiative diffusion promotes spike compression and bubble expansion, thereby intensifying the instability development.

Regarding radiation pressure, increasing radiation pressure is physically equivalent to elevating the medium's sound speed, which inhibits spike compression and bubble expansion. As shown in Fig. 7, the amplitude of velocity divergence decreases with reducing Mihalas number. When the Mihalas number approaches zero, the system enters an incompressible regime. Compared to the adiabatic conditions, this results in lower spike density and higher bubble density, leading to reduced buoyancy effects and consequently smaller perturbation growth rates.

In summary, both radiative diffusion and radiation pressure alter the RTI growth rate by influencing the compressibility of spikes and the expandability of bubbles.

C. Impact of key physical parameters

To assess the generality of the identified radiation effects, this section explores their dependence on the fundamental parameters of the system: stratification strength (Sr), Atwood number (At), radiative thermal conductivity contrast (A_κ), and interface thickness (δ).

Figure 8 presents the squared growth rate as a function of stratification strength for Atwood numbers At $= 0.25$, 0.5, and 0.9. Solid lines mark the adiabatic, isothermal and incompressible limits. Across all At and Sr values, the radiative influence identified in Sec. III A is preserved: lowering the Péclet number (while keeping the Mihalas number at 10^6) drives the growth rate from the adiabatic toward the isothermal limit, whereas reducing the Mihalas number (at fixed Pe $= 10^6$) pushes it from the adiabatic toward the incompressible limit. Notably, the rapid variation of the growth rate with Pe and R occurs only in the interval $10^{-2} \lesssim$ Pe, $R \lesssim 10^2$, signifying

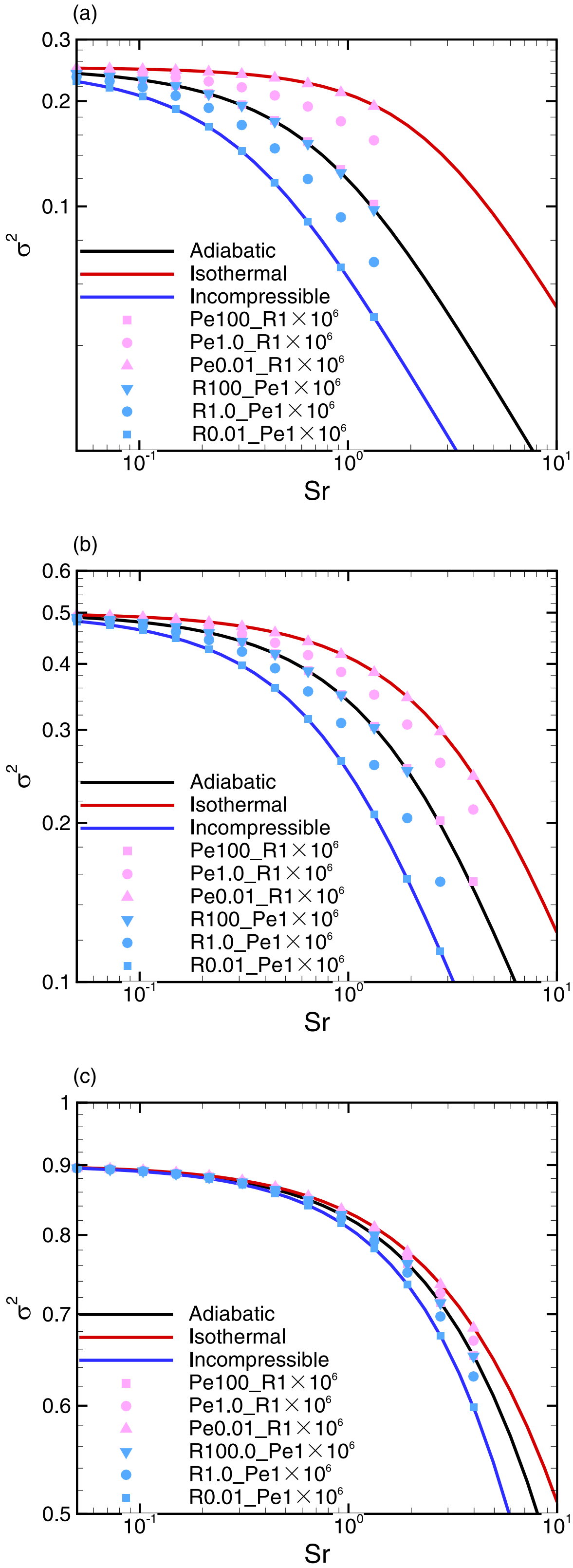

FIG. 8. Squared growth rate for different stratified parameter Sr and Atwood number: (a) At $= 0.25$, (b) At $= 0.5$, and (c)At $= 0.9$.

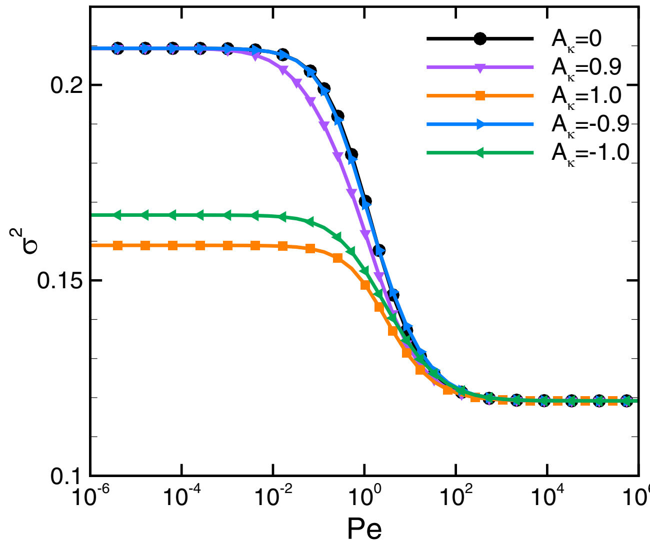

FIG. 9. Squared growth rate σ^2 as a function of Pe number for different radiative conductivity contrasts A_κ.

that these two dimensionless groups are excellent indicators of radiative effects.

Comparison across parameter space in Fig. 8 demonstrates that radiation effects are more pronounced at stronger stratification and smaller Atwood numbers. Furthermore, the results in Fig. 8 demonstrate that the dependence of RTI growth rates on stratification strength is modulated by radiation effects. Compared to the classical case, enhanced radiative diffusion reduces the sensitivity of growth rates to stratification strength, whereas increased radiation pressure amplifies this dependence.

Previous analyses assumed identical radiative thermal conductivity (κ) for both medium ($A_\kappa = 0$), yet practical systems often exhibit significant κ contrast, differing by orders of magnitude in extreme cases [32]. Figure 9 compares the squared growth rates of RTI versus Pe number across different conductivity-contrast parameters A_κ. The results demonstrate that κ-contrast weakens the influence of radiative diffusion, evidenced by the flattening of σ^2 versus Pe curves with increasing $|A_\kappa|$.

For extreme negative contrast ($A_\kappa = -1$), radiative diffusion localizes exclusively in the light medium, reducing asymptotic growth rates. Conversely, under extreme positive contrast ($A_\kappa = 1$), diffusion is confined solely to the heavy medium, causing further reduction in asymptotic σ^2. This indicates that radiative diffusion in the light medium exerts stronger modulation on RTI growth than in the heavy medium.

Previous analyses set the pseudo-interface thickness of the mean flow to $\delta = 10^{-3}$, yielding results approaching those of a sharp interface. We investigated the δ dependence, with Fig. 10 showing perturbation squared growth rates versus δ at At $= 0.25$, Sr $= 1.0$, and $R = 10^6$ for various Péclet numbers. When $\delta < 10^{-2}$, the RTI growth rate approaches that of a sharp interface. Increasing δ suppresses RTI growth. For cases with negligible radiative diffusion (large Pe), perturbations cease growing when δ is sufficiently large. As shown in the inset of Fig. 10, this suppression occurs because increasing δ smooths the initial density jump at the interface, thereby violating the classical Rayleigh-Taylor instability criterion. However, under strong radiative diffusion (small Pe), the RTI growth rate remains positive even with a smoothed interface.

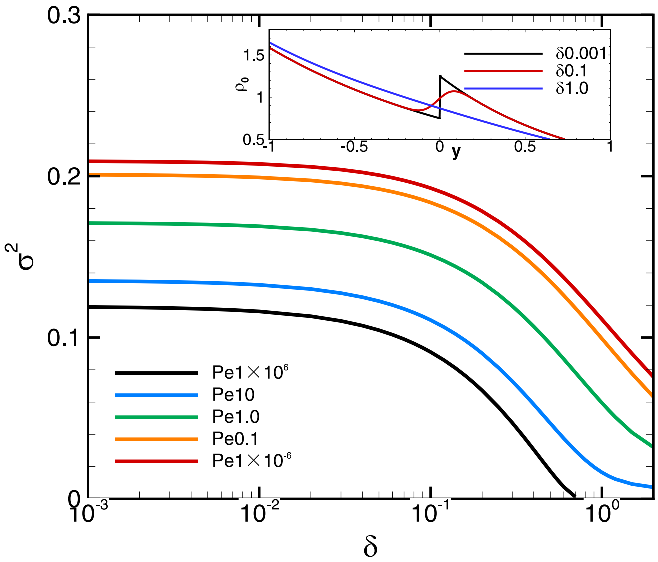

FIG. 10. Squared growth rate σ^2 as a function of pseudo-interface thickness δ for different Pe number. The inset shows the density profiles of the background state for different pseudo-interface thicknesses δ.

These results align with the modified instability criterion proposed by Chkair [31] for large δ at low Pe.

IV. CONCLUSION

Radiation is a primary energy-transport channel in HED flows. To explore its specific influence on the RTI, we have performed a linear stability analysis. Within the equilibrium-diffusion approximation, this work extends the classical framework of Livescu [17] to the HED regime, systematically quantifying how finite radiative diffusion (low Péclet number, Pe $\lesssim 1$) and significant radiation pressure (low Mihalas number, $R \lesssim 1$) jointly reshape the linear growth of the compressible RTI.

Our analysis demonstrates that the two radiative mechanisms competitively modulate the instability by altering the effective fluid compressibility. Radiative heat diffusion enhances compressibility, driving the growth rate from the adiabatic toward the isothermal limit. Conversely, radiation pressure reduces compressibility, steering the growth rate toward the incompressible limit. These effects are governed by the key dimensionless parameters Pe (ratio of convective to diffusive transport) and R (ratio of material to radiation pressure). A parametric study across Atwood number (At), stratification strength (Sr), and interface thickness (δ) further reveals that the radiative impact is most pronounced for systems with low At, high Sr, or large δ.

Finally, our analysis assumes preexisting thermal equilibrium and equilibrium-diffusion transport. While this excludes systems with strong temperature gradients (e.g., classical shock structures or ICF ablation fronts), the equilibrium-diffusion approximation warrants caution in the upper-left region of the Pe-R parameter space where $R/\mathrm{Pe} \gg 1$. Nevertheless, the radiation-modulated compressibility mechanism identified here offers a robust general picture of RTI across the explored parameter regimes.

ACKNOWLEDGMENTS

This work was supported by the Foundation of National Key Laboratory of Computational Physics (Grant No. JKRW2025-05), Science Challenge Project (Grant No. TZ2025016), and National Natural Science Foundation of China (Grants No. 12375235 and No. 12202070).

DATA AVAILABILITY

The data that support the findings of this article are not publicly available upon publication because it is not technically feasible and/or the cost of preparing, depositing, and hosting the data would be prohibitive within the terms of this research project. The data are available from the authors upon reasonable request.

APPENDIX A: FORMULATION OF MATRICES IN EQ. (32)

The matrices $\mathbf{V}$, $\mathbf{V}_x$, $\mathbf{V}_{xx}$, $\mathbf{V}_y$, $\mathbf{V}_{yy}$, and $\mathbf{V}_t$ are formulated as

$$\mathbf{V} = \begin{bmatrix} 0 & 0 & \partial_y \rho_0 & 0 & 0 \\ 0 & 0 & 0 & 0 & 0 \\ 1 + \partial_y(\partial_\rho p_0)/S_r & 0 & 0 & \partial_y(\partial_T p_0)/\mathrm{Sr} & \partial_y(\partial_c p_0)/\mathrm{Sr} \\ 0 & 0 & 0 & 0 & 0 \\ 0 & 0 & \partial_y c_0 & 0 & 0 \end{bmatrix}, \tag{A1}$$

$$\mathbf{V}_x = \begin{bmatrix} 0 & \rho_0 & 0 & 0 & 0 \\ \partial_\rho p_0/\mathrm{Sr} & 0 & 0 & \partial_T p_0/\mathrm{Sr} & \partial_c p_0/\mathrm{Sr} \\ 0 & 0 & 0 & 0 & 0 \\ 0 & (\gamma_{2,0} - 1)T_0 & 0 & 0 & 0 \\ 0 & 0 & 0 & 0 & 0 \end{bmatrix}, \tag{A2}$$

$$\mathbf{V}_y = \begin{bmatrix} 0 & 0 & \rho_0 & 0 & 0 \\ 0 & 0 & 0 & 0 & 0 \\ \partial_\rho p_0/\mathrm{Sr} & 0 & 0 & \partial_T p_0/\mathrm{Sr} & \partial_c p_0/\mathrm{Sr} \\ 0 & 0 & (\gamma_{2,0} - 1)T_0 & \frac{-\partial_y \kappa_0}{\mathrm{Pe}\rho_0 C_{V,0}} & 0 \\ 0 & 0 & 0 & 0 & 0 \end{bmatrix}, \tag{A3}$$

$$\mathbf{V}_{xx} = \begin{bmatrix} 0 & 0 & 0 & 0 & 0 \\ 0 & 0 & 0 & 0 & 0 \\ 0 & 0 & 0 & 0 & 0 \\ 0 & 0 & 0 & \frac{-\kappa_0}{\mathrm{Pe}\rho_0 C_{V,0}} & 0 \\ 0 & 0 & 0 & 0 & 0 \end{bmatrix}, \tag{A4}$$

$$\mathbf{V}_{yy} = \begin{bmatrix} 0 & 0 & 0 & 0 & 0 \\ 0 & 0 & 0 & 0 & 0 \\ 0 & 0 & 0 & 0 & 0 \\ 0 & 0 & 0 & -\frac{\kappa_0}{\mathrm{Pe}\rho_0 C_{V,0}} & 0 \\ 0 & 0 & 0 & 0 & 0 \end{bmatrix}, \tag{A5}$$

TABLE I. Validation of the squared RTI growth rate against analytical reference solutions for interface thicknesses $\delta = 10^{-2},\ 10^{-3},\ 10^{-4}$. Relative errors are given in parentheses.

Sr	0.001	0.01	0.1	0.5	1.0	2.0
Ref.	0.24980	0.24796	0.23038	0.16822	0.11920	0.07108
$\delta = 10^{-2}$	0.24790	0.24605	0.22833	0.16564	0.11617	0.06765
	(−0.759%)	(−0.770%)	(−0.886%)	(−1.531%)	(−2.544%)	(−4.815%)
$\delta = 10^{-3}$	0.24960	0.24777	0.23017	0.16796	0.11890	0.07073
	(−0.077%)	(−0.077%)	(−0.089%)	(−0.154%)	(−0.256%)	(−0.486%)
$\delta = 10^{-4}$	0.24977	0.24794	0.23036	0.16819	0.11917	0.07104
	(−0.008%)	(−0.008%)	(−0.009%)	(−0.016%)	(−0.025%)	(−0.048%)

$$\mathbf{V}_t = \begin{bmatrix} 1 & 0 & 0 & 0 & 0 \\ 0 & \rho_0 & 0 & 0 & 0 \\ 0 & 0 & \rho_0 & 0 & 0 \\ 0 & 0 & 0 & 1 & 0 \\ 0 & 0 & 0 & 0 & 1 \end{bmatrix}. \tag{A6}$$

APPENDIX B: VALIDATION AGAINST ANALYTICAL SOLUTIONS FOR NONRADIATIVE COMPRESSIBLE RTI

Results of the linear stability analysis are validated against the analytical solutions of Livescu [17] for the nonradiative case. To facilitate the comparison, we recast the dispersion relation derived by Livescu in terms of the symbols defined in the present paper:

$$\begin{aligned}(1-\mathrm{At})[\gamma^{\mathrm{m}} + \sigma^2(1+\mathrm{At})\mathrm{Sr}](\sigma^2\lambda_L + 1) \\ = (1+\mathrm{At})[\gamma^{\mathrm{m}} + \sigma^2(1-\mathrm{At})\mathrm{Sr}](\sigma^2\lambda_H + 1),\end{aligned} \tag{B1}$$

where λ_H, λ_L are given by

$$\begin{aligned}\lambda_L &= \frac{(1-\mathrm{At})\mathrm{Sr}}{2} + \sqrt{\frac{(1-\mathrm{At})^2\mathrm{Sr}^2}{4} + 1 + \frac{(1-\mathrm{At})\mathrm{Sr}\sigma^2}{\gamma^{\mathrm{m}}} + \frac{(1-\mathrm{At})(\gamma^{\mathrm{m}}-1)\mathrm{Sr}}{\gamma^{\mathrm{m}}\sigma^2}} \\ \lambda_H &= \frac{(1+\mathrm{At})\mathrm{Sr}}{2} - \sqrt{\frac{(1+\mathrm{At})^2\mathrm{Sr}^2}{4} + 1 + \frac{(1+\mathrm{At})\mathrm{Sr}\sigma^2}{\gamma^{\mathrm{m}}} + \frac{(1+\mathrm{At})(\gamma^{\mathrm{m}}-1)\mathrm{Sr}}{\gamma^{\mathrm{m}}\sigma^2}}.\end{aligned} \tag{B2}$$

Shape function of vertical velocity:

$$\hat{v} = \begin{cases} Ce^{\lambda_L y} & y < 0 \\ Ce^{\lambda_H y} & y > 0 \end{cases}, \tag{B3}$$

where C is a constant.

Shape function of pressure $\hat{p}$

$$\hat{p} = \frac{\sigma \mathrm{Sr} \rho_0}{k^2 + S_r\sigma^2/a_0^2}\left(\frac{\mathrm{Sr}\hat{v}}{a_0^2} - \frac{\partial \hat{v}}{\partial y}\right), \tag{B4}$$

where $a_0^2 = \gamma^{\mathrm{m}} p_0/\rho_0$.

Shape function of $\hat{u}$

$$\hat{u} = -\frac{ik}{\mathrm{Sr}}\frac{\hat{p}}{\sigma\rho_0} = \frac{-ik}{k^2 + \mathrm{Sr}\sigma^2/a_0^2}\left(\frac{\mathrm{Sr}\hat{v}}{a_0^2} - \frac{\partial \hat{v}}{\partial y}\right). \tag{B5}$$

Shape function of density $\hat{\rho}$

$$\begin{aligned}\hat{\rho} &= -\sigma\rho_0\hat{v} - \frac{1}{\mathrm{Sr}}\frac{\partial \hat{p}}{\partial y} \\ &= -\sigma\rho_0\hat{v} - \frac{\sigma\rho_0}{k^2 + \mathrm{Sr}\sigma^2/a_0^2}\left(\frac{\mathrm{Sr}}{a_0}\frac{\partial \hat{v}}{\partial y} - \frac{\partial^2 \hat{v}}{\partial y^2}\right) \\ &\quad - \frac{\sigma}{k^2 + \mathrm{Sr}\sigma^2/a_0^2}\left(\frac{\mathrm{Sr}\hat{v}}{a_0^2} - \frac{\partial \hat{v}}{\partial y}\right)\frac{\partial \rho_0}{\partial y}.\end{aligned} \tag{B6}$$

We set the Atwood number to At = 0.25 and compare the squared growth rate against the stratification parameter Sr. The Péclet number is fixed at Pe $= 10^6$ and the Mihalas number at $R = 10^6$, so that radiative effects are eliminated. Small interface thicknesses ($\delta = 10^{-2}, 10^{-3}, 10^{-4}$) are selected to approach the sharp-interface analytical limit.

Table I demonstrates that for nonradiative cases, the squared RTI growth rate derived from LSA exhibits excellent agreement with analytical reference solutions. The relative deviation between LSA and analytical results decreases proportionally with reduced δ, falling below 0.5% at $\delta = 10^{-3}$, the value adopted in this study.

Figure 11 presents perturbation eigenfunctions for Sr = 1.0, demonstrating excellent agreement with the analytical reference solutions. Analytical studies assume a density discontinuity at the interface, whereas the present approach employs a smooth transition treatment. Within this smoothing region, the steep stationary density gradient produces locally amplified $\hat{\rho}$ amplitudes. Crucially, the solution outside the smoothing region remains unaffected.

APPENDIX C: CONVERGENCE VALIDATION

To verify the convergence of the LSA with respect to the computational grid, Fig. 12 compares solutions obtained

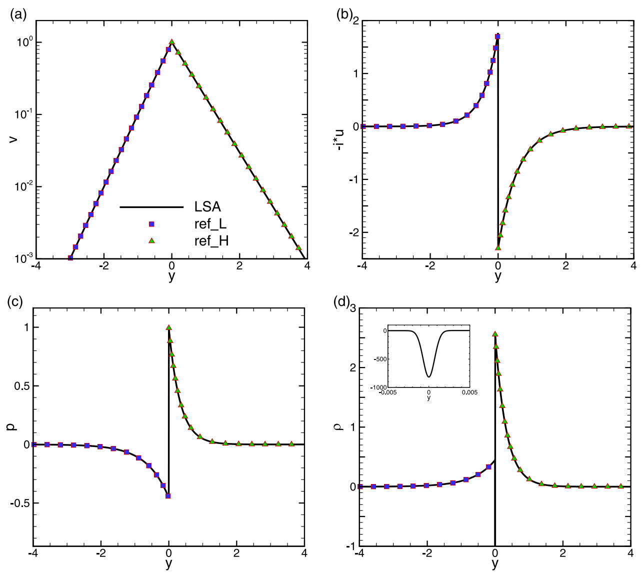

FIG. 11. Validation of (a) $\hat{v}$, (b) $\hat{u}$, (c) $\hat{p}$, and (d) $\hat{\rho}$ against reference analytical solutions.

with domain heights ($L_y = 5.0, 7.5, 10.0$) and grid resolutions ($n_y = 500, 1000, 2000$) at $\mathrm{Sr} = 1.0$ and $R = 10^6$. The LSA-derived growth rates exhibit excellent consistency throughout the tested parameter space. Figure 12(b) compares eigenfunctions at $\mathrm{Pe} = 10^{-6}$. Compared with the $\mathrm{Pe} = 10^6$ case [Fig. 11(a)], the eigenfunction decays more slowly along y, so the boundary conditions imposed at $y = L_y$ exert a stronger influence on the perturbation eigenfunction. Although a larger L_y mitigates this boundary effect, it introduces convergence difficulties at high Sr. We adopt $L_y = 7.5$ as a compromise between convergence and computational cost; the deviations occur only in regions where the eigenfunction amplitude is already below 1% of its maximum. Consequently, the chosen grid parameters ($L_y = 7.5$, $n_y = 1000$) introduce negligible uncertainty into the LSA results.

APPENDIX D: PARAMETER RELEVANCE

To validate the practical relevance of our explored parameter space, we provide estimates of the characteristic Pe and R values across real systems, along with a parameter survey.

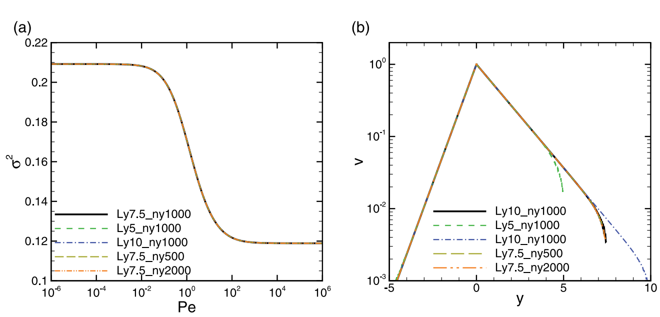

FIG. 12. Convergence study at fixed $\mathrm{Sr} = 1.0$, $R = 10^6$: (a) squared growth rate versus Pe for domain heights $L_y = 5.0$, 7.5, 10.0 and grid resolutions $n_y = 500$, 1000, 2000; (b) corresponding shape function $\hat{v}$ at $\mathrm{Pe} = 10^{-6}$.

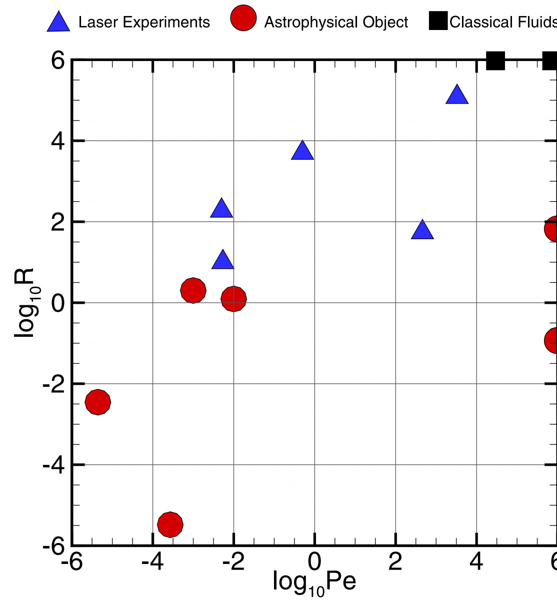

FIG. 13. (Pe, R) parameter space with annotated data points from Classical Fluid, Astrophysical Object, and Laser Experiment systems. Corresponding system details are provided in Table II.

Based on the definitions of Pe and R:

$$\mathrm{Pe} \propto \frac{\sqrt{T}L}{\kappa} \propto L\rho^{1-\alpha}T^{-\beta},$$
$$R \propto \rho T^{-3}, \tag{D1}$$

where the sound velocity is adopted as the characteristic velocity. Literature values for high-energy-density plasmas [32,40] indicate $\alpha \in [-1, -2]$ and $\beta \in [4, 7]$.

Elevated temperatures and reduced densities generally yield very small Pe and R values. Additionally, the multiparameter dependence on ρ and L allows extreme combinations to be achieved through distinct physical pathways: large R with small Pe is achievable in high-temperature, low-density, small-scale systems like laser-heated plasmas, while small R with large Pe occurs in low-temperature, high-density, large-scale environments such as stellar interiors.

Table II surveys representative systems, while Fig. 13 overlays corresponding (Pe, R) data points onto our parameter space. This demonstrates the feasibility of extreme R and Pe values across classical, astrophysical, and laboratory regimes. Importantly, while the specific systems surveyed may not focus exclusively on RTI, literature reports [7,33] indicate that RTI is a significant potential source of instability in such environments.

The equilibrium-diffusion approximation adopted in the present research assumes the photon mean-free path (l^{r}) is short compared to the characteristic length scale of the system (L), establishing local thermal equilibrium through a single temperature field. The radiative thermal conductivity is given by $\kappa = 4acT^3 l^{\mathrm{r}}/3$, where c denotes the speed of light [32]. By combining the definitions of the Péclet number and the Mihalas number, and applying the equations of state, we derive

$$\frac{l^{\mathrm{r}}}{L} = \frac{R}{\mathrm{Pe}}\frac{u}{4c}. \tag{D2}$$

TABLE II. Characteristic Péclet (Pe) and Mihalas (R) numbers for different physical systems.

Category	Problem (references)	Pe	R
Classical fluids	Rayleigh-Taylor instability [48]	3×10^4	$\gg 10^{6}$[b]
Classical fluids	Reshock experiments [49,50]	7.6×10^5	$\gg 10^{6}$[b]
Astrophysical objects	SN 1987A He-H interface [32]	1.0×10^6	0.12
Astrophysical objects	Supernova shock breakout [40,51]	2.7×10^{-4}	3.3×10^{-6}
Astrophysical objects	Herbig-Haro objects [40,52]	4.4×10^{-6}	3.5×10^{-3}[b]
Astrophysical objects	Solar interior [53,54]	10^6–10^7	65.7
Astrophysical objects	Outer layers of $10M_\odot$ Stars [54,55]	1.0×10^{-3}	2.0
Astrophysical objects	Interior of massive stars [31]	1.0×10^{-2}	1.24
Laser experiments	Supersonic jets [40,52]	460	54.7[b]
Laser experiments	Radiative shocks [40,51]	0.5	5.0×10^3
Laser experiments	Radiative shocks [56]	5.4×10^{-3}[a]	10.0
Laser experiments	Reshock experiments [50]	3.3×10^3	1.2×10^{5}[b]
Laser experiments	Direct-drive fusion ignition [57]	5.0×10^{-3}[a]	1.87×10^{2}[b]

Note: Due to the lack of directly reported values of Pe and R in the literature, some entries are estimated from the density and temperature data provided in the references.
[a]Estimated Pe based on density, temperature, and opacity [32,40].
[b]Estimated R based on density and temperature.

The equilibrium-diffusion approximation may become quantitatively inaccurate when R/Pe is large and exceeds $4c/u$. Given that $4c/u$ typically represents a large value, the approximation generally remains valid. However, its accuracy may diminish in the upper-left region of the Pe-R parameter space. Furthermore, the thermal equilibrium background assumption renders the model inapplicable to systems with strong temperature gradients, such as shock structures or ICF ablation fronts.

[1] Lord Rayleigh, Investigation of the Character of the Equilibrium of an Incompressible Heavy Fluid of Variable Density, Proc. London Mathe. Soc. **s1-14**, 170 (1882).

[2] G. I. Taylor, The instability of liquid surfaces when accelerated in a direction perpendicular to their planes. I, Proc. R. Soc. A **201**, 192 (1950).

[3] J. F. Adkins, K. McIntyre, and D. P. Schrag, The salinity, temperature, and δ^{18}O of the glacial deep ocean, Science **298**, 1769 (2002).

[4] C. Wunsch and R. Ferrari, Vertical mixing, energy, and the general circulation of the oceans, Annu. Rev. Fluid Mech. **36**, 281 (2004).

[5] T. K. Nymark, C. Fransson, and R. A. Chevalier, Radio and x-ray emission as probes of type IIP supernovae and red supergiant mass loss, Astrophys. J. **641**, 1029 (2006).

[6] C. C. Kuranz, H.-S. Park, C. M. Huntington, A. R. Miles, B. A. Remington, T. Plewa, M. R. Trantham, H. F. Robey, D. Shvarts, A. Shimony, *et al.*, How high energy fluxes may affect Rayleigh–Taylor instability growth in young supernova remnants, Nat. Commun. **9**, 1564 (2018).

[7] Y. Zhou, Rayleigh–Taylor and Richtmyer–Meshkov instability induced flow, turbulence, and mixing. I, Phys. Rep. **720–722**, 1 (2017).

[8] Y. Zhou, Rayleigh–Taylor and Richtmyer–Meshkov instability induced flow, turbulence, and mixing. II, Phys. Rep. **723–725**, 1 (2017).

[9] I. B. Bernstein and D. L. Book, Effect of compressibility on the Rayleigh–Taylor instability, Phys. Fluids **26**, 453 (1983).

[10] Y. Yang and Q. Zhang, General properties of a multilayer stratified fluids system, Phys. Fluids A **5**, 1167 (1993).

[11] L. Turner, Rayleigh-Taylor instabilities and gravity waves in compressible fluids, Technical Report No. LA-UR-02-6439, Los Alamos National Laboratory, Los Alamos, NM, 2002.

[12] G. M. Blake, Fluid dynamic stability of double radio sources, Mon. Not. R. Astron. Soc. **156**, 67 (1972).

[13] D. H. Sharp, An overview of Rayleigh-Taylor instability, Physica D **12**, 3 (1984).

[14] X. L. Li, Study of three-dimensional Rayleigh–Taylor instability in compressible fluids through level set method and parallel computation, Phys. Fluids A **5**, 1904 (1993).

[15] L. Baker, Compressible Rayleigh–Taylor instability, Phys. Fluids **26**, 950 (1983).

[16] C. S. Qin, P. Wang, F. G. Zhang, Rayleigh-taylor and kelvinhelmholtz instability of compressible fluid, J. Theor. Appl. Mech. **36**, 655 (2004).

[17] D. Livescu, Compressibility effects on the Rayleigh–Taylor instability growth between immiscible fluids, Phys. Fluids **16**, 118 (2004).

[18] T. Luo, J. Wang, C. Xie, M. Wan, and S. Chen, Effects of compressibility and Atwood number on the single-mode Rayleigh-Taylor instability, Phys. Fluids **32**, 012110 (2020).

[19] P. O. Vandervoort, The character of the equilibrium of a compressible, inviscid fluid of varying density, Astrophys. J. **134**, 699 (1961).

[20] M. S. Plesset and A. Prosperetti, Reply to comments on "General analysis of the stability of superposed fluids", Phys. Fluids **25**, 911 (1982).

[21] X. Ribeyre, V. T. Tikhonchuk, and S. Bouquet, Compressible RayleighTaylor instabilities in supernova remnants, Phys. Fluids **16**, 4661 (2004).

[22] J. I. Castor, *Radiation Hydrodynamics* (Cambridge University Press, Cambridge, 2004).
[23] S. Atzeni and J. M. ter Vehn, *The Physics of Inertial Fusion* (Oxford University Press, Oxford, 2004).
[24] J. Sanz, Self-consistent analytical model of the Rayleigh-Taylor instability in inertial confinement fusion, Phys. Rev. Lett. **73**, 2700 (1994).
[25] V. N. Goncharov, R. Betti, R. L. McCrory, P. Sorotokin, and C. P. Verdon, Self-consistent stability analysis of ablation fronts with large Froude numbers, Phys. Plasmas **3**, 1402 (1996).
[26] S. Fujioka, A. Sunahara, K. Nishihara, N. Ohnishi, T. Johzaki, H. Shiraga, K. Shigemori, M. Nakai, T. Ikegawa, M. Murakami, *et al.*, Suppression of the Rayleigh-Taylor instability due to self-radiation in a multiablation target, Phys. Rev. Lett. **92**, 195001 (2004).
[27] J. Li, R. Yan, B. Zhao, J. Zheng, H. Zhang, and X. Lu, Mitigation of the ablative Rayleigh–Taylor instability by nonlocal electron heat transport, Matter Radiat. Extremes **7**, 055902 (2022).
[28] E. Jacquet and M. R. Krumholz, Radiative Rayleigh-Taylor instabilities, Astrophys. J. **730**, 116 (2011).
[29] Z.-X. Hu, Y.-S. Zhang, and B.-L. Tian, Evolution of Rayleigh-Taylor instability under interface discontinuous acceleration induced by radiation, Phys. Rev. E **101**, 043115 (2020).
[30] P. Tremblin, H. Bloch, M. González, E. Audit, S. Fromang, T. Padioleau, P. Kestener, and S. Kokh, Radiative Rayleigh-Taylor instability and the structure of clouds in planetary atmospheres, Astron. Astrophys. **653**, A30 (2021).
[31] J.-C. Chkair, O. Soulard, J. Griffond, and X. Blanc, Small-Péclet-number approximation for stellar turbulent mixing zones, Phys. Rev. E **102**, 033111 (2020).
[32] R. P. Drake, *High Energy Density Physics: Fundamentals, Inertial Fusion and Experimental Astrophysics* (Springer, New York, 2018).
[33] P. Garaud, Journey to the center of stars: The realm of low Prandtl number fluid dynamics, Phys. Rev. Fluids **6**, 030501 (2021).
[34] E. A. Spiegel, Thermal turbulence at very small Prandtl number, J. Geophys. Res. **67**, 3063 (1962).
[35] L. Cope, P. Garaud, and C. P. Caulfield, The dynamics of stratified horizontal shear flows at low Péclet number, J. Fluid Mech. **903**, A1 (2020).
[36] P. Garaud, Double-diffusive convection at low Prandtl number, Annu. Rev. Fluid Mech. **50**, 275 (2018).
[37] D. Mihalas and B. W. Mihalas, *Foundations of Radiation Hydrodynamics* (Dover, New York, 2013).
[38] P. G. Drazin and W. H. Reid, *Hydrodynamic Stability*, 2nd ed. (Cambridge University Press, Cambridge, 2004).
[39] Y. B. Zel'dovich and Y. P. Raizer, *Physics of Shock Waves and High-Temperature Hydrodynamic Phenomena* (Academic Press, New York, 1966).
[40] J. E. Cross, B. Reville, and G. Gregori, Scaling of magneto-quantum-radiative hydrodynamic equations: From laser-produced plasmas to astrophysics, Astrophys. J. **795**, 59 (2014).
[41] S. Gauthier, Compressible Rayleigh–Taylor turbulent mixing layer between Newtonian miscible fluids, J. Fluid Mech. **830**, 211 (2017).
[42] S. J. Reckinger, D. Livescu, and O. V. Vasilyev, Comprehensive numerical methodology for direct numerical simulations of compressible Rayleigh-Taylor instability, J. Comput. Phys. **313**, 181 (2016).
[43] C.-Q. Fu, Z. Zhao, P. Wang, N.-S. Liu, Z.-H. Wan, and X.-Y. Lu, Bubble re-acceleration behaviours in compressible Rayleigh–Taylor instability with isothermal stratification, J. Fluid Mech. **954**, A16 (2023).
[44] M. A. Lafay, B. L. Creurer, and S. Gauthier, Compressibility effects on the Rayleigh-Taylor instability between miscible fluids, Europhys. Lett. **79**, 64002 (2007).
[45] R. B. Lehoucq, D. C. Sorensen, and C. Yang, *ARPACK Users' Guide: Solution of Large-Scale Eigenvalue Problems with Implicitly Restarted Arnoldi Methods* (SIAM, Philadelphia, 1998).
[46] L. Han, J. Yuan, M. Dong, and Z. Fan, Secondary instability of the spike-bubble structures induced by nonlinear Rayleigh-Taylor instability with a diffuse interface, Phys. Rev. E **104**, 035108 (2021).
[47] C. Almarcha, P. Clavin, L. Duchemin, and J. Sanz, Ablative Rayleigh-Taylor instability with strong temperature dependence of the thermal conductivity, J. Fluid Mech. **579**, 481 (2007).
[48] W. H. Cabot and A. W. Cook, Reynolds number effects on Rayleigh–Taylor instability with possible implications for type Ia supernovae, Nat. Phys. **2**, 562 (2006).
[49] D. J. Hill, C. Pantano, and D. I. Pullin, Large-eddy simulation and multiscale modelling of a Richtmyer–Meshkov instability with reshock, J. Fluid Mech. **557**, 29 (2006).
[50] J. D. Bender, O. Schilling, K. S. Raman, R. A. Managan, B. J. Olson, S. R. Copeland, C. L. Ellison, D. J. Erskine, C. M. Huntington, B. E. Morgan, *et al.*, Simulation and flow physics of a shocked and reshocked high-energy-density mixing layer, J. Fluid Mech. **915**, A84 (2021).
[51] A. Pak, L. Divol, G. Gregori, S. Weber, J. Atherton, R. Bennedetti, D. K. Bradley, D. Callahan, D. T. Casey, E. Dewald, *et al.*, Radiative shocks produced from spherical cryogenic implosions at the National Ignition Facility, Phys. Plasmas **20**, 056315 (2013).
[52] V. T. Tikhonchuk, P. Nicola, X. Ribeyre, C. Stenz, G. Schurtz, A. Kasperczuk, T. Pisarczyk, L. Juha, E. Krousky, K. Masek, *et al.*, Laboratory modeling of supersonic radiative jets propagation in plasmas and their scaling to astrophysical conditions, Plasma Phys. Controlled Fusion **50**, 124056 (2008).
[53] Z.-L. Guo and Y. Li, Study on properties of the k-ω model for stellar convection, Chin. Astron. Astrophys. **38**, 413 (2014).
[54] R. Kippenhahn, A. Weigert, and A. Weiss, *Stellar Structure and Evolution* (Springer, New York, 2013).
[55] P. Garaud, Turbulent transport in a strongly stratified forced shear layer with thermal diffusion, Astrophys. J. **821**, 49 (2016).
[56] T. Michel, B. Albertazzi, P. Mabey, G. Rigon, F. Lefevre, L. Van Box Som, P. Barroso, S. Egashira, R. Kumar, C. Michaut, *et al.*, Laboratory observation of radiative shock deceleration and application to SN 1987A, Astrophys. J. **888**, 25 (2020).
[57] K. Molvig, M. J. Schmitt, B. J. Albright, E. S. Dodd, N. M. Hoffman, G. H. McCall, and S. D. Ramsey, Low fuel convergence path to direct-drive fusion ignition, Phys. Rev. Lett. **116**, 255003 (2016).